Measurement of the cosmic ray spectrum above 4×10^{18} eV using inclined events detected with the Pierre Auger Observatory

Measurement of the cosmic ray spectrum above 4×10^{18} eV using inclined events detected with the Pierre Auger Observatory

The Pierre Auger collaboration

E-mail: auger_spokespersons@fnal.gov

Abstract. A measurement of the cosmic-ray spectrum for energies exceeding 4×10^{18} eV is presented, which is based on the analysis of showers with zenith angles greater than $60°$ detected with the Pierre Auger Observatory between 1 January 2004 and 31 December 2013. The measured spectrum confirms a flux suppression at the highest energies. Above 5.3×10^{18} eV, the "ankle", the flux can be described by a power law $E^{-\gamma}$ with index $\gamma = 2.70 \pm 0.02\,(\text{stat}) \pm 0.1\,(\text{sys})$ followed by a smooth suppression region. For the energy (E_{s}) at which the spectral flux has fallen to one-half of its extrapolated value in the absence of suppression, we find $E_{\text{s}} = (5.12 \pm 0.25\,(\text{stat})^{+1.0}_{-1.2}\,(\text{sys})) \times 10^{19}$ eV.

Contents

1 Introduction

The Pierre Auger Observatory is to date the largest detector of air showers induced by the ultra-high energy cosmic rays (UHECRs). It is a hybrid detector combining an array of surface detectors (SD), that measures the particle densities in the shower at the ground, and a fluorescence detector (FD), that captures the ultraviolet light emitted by nitrogen as showers develop in the atmosphere. The SD [1, 2], spread over an area of $3000\,km^2$, is composed of a baseline array, comprising more than 1600 water-Cherenkov detectors placed in a hexagonal grid with nearest neighbours separated by 1500 m. The FD [3] comprises 24 fluorescence telescopes distributed in 4 perimeter buildings which view the atmosphere over the array. The site is located near Malargüe, Province of Mendoza, Argentina, at an altitude of about 1400 m above sea level and at an average geographic latitude of $35.2°\,S$. The redundancy provided by the two detection techniques has proved to be extremely valuable for a wide range of applications and has improved the performance of the Observatory beyond expectations.

The data gathered at the Pierre Auger Observatory with zenith angles less than $60°$ have provided a measurement of the UHECR spectrum [4] with unprecedented statistics. The technique developed exploits the large aperture of the SD, operating continuously, as well as the calorimetric measurement of the energy deposit obtained with the FD which is, by contrast, rather limited in duty cycle to clear nights without moonlight (13%). A parameter quantifying the shower size is obtained from the SD. This parameter is then calibrated using the energy inferred from the calorimetric FD measurement for a sub-sample of the events (hybrid events) which are detected and reconstructed simultaneously with both techniques [4]. This allows measurements of the energy spectrum with an energy estimation weakly reliant upon shower simulations. The spectrum obtained is consistent with the Greisen and Zatsepin-Kuz'min (GZK) suppression [5, 6]. The observation of this strong flux suppression was first reported by HiRes [7]. In addition, the spectrum has been independently measured using hybrid events which are detected with the fluorescence technique and at least one particle detector [8]. The latter measurement has also been combined with the SD spectrum to obtain a spectrum extending to lower energies [8, 9], which has confirmed the flattening of the spectral slope at about $5 \times 10^{18}\,eV$, often referred to as the "ankle". Similarly the

Telescope Array (TA) experiment [10, 11], having an array of scintillators spread over an area of $700\,\text{km}^2$, together with fluorescence telescopes, has provided an independent measurement of the spectrum using showers with zenith angles less than $45°$ in the Northern Hemisphere, which clearly displays the GZK steepening [12]. Although the two spectra are in agreement between the ankle and $5\times10^{19}\,\text{eV}$, there are discrepancies in the suppression region which are being scrutinized by a joint working group of both Collaborations.

The choice of deep-water Cherenkov detectors for the Pierre Auger Observatory was made to give substantial solid angle coverage for zenith angles exceeding $60°$ thus enabling detection of showers over a much broader angular and declination range than is possible in arrays using thinner detectors. The showers with large zenith angles traverse much larger atmospheric depths than than showers nearer the vertical and, as a result, are characterised by the dominance of secondary energetic muons at the ground, since the electromagnetic component of the shower is largely absorbed before reachig ground. Inclined showers have been observed since the 1960s and have stirred much interest [13], but the first reliable methods for event reconstruction are relatively recent [14, 15]. These events provide an independent measurement of the cosmic-ray spectrum. In addition, since inclined showers are mainly composed by muons, their analysis has been shown to be particularly useful in determining the muon content of showers for comparison with predictions from shower models [16]. Inclined showers are also used to extend the accessible fraction of the sky covered in analyses of the distribution of the arrival directions of cosmic rays detected at Auger [17, 18] and constitute the main background for searches for ultra-high energy neutrinos using air showers [19].

In this article we present the measurement of the cosmic-ray spectrum derived from events with zenith angles between $60°$ and $80°$ detected with the Pierre Auger Observatory in the time period from 1 January 2004 to 31 December 2013.

2 Estimation of the shower energy

Since inclined showers are dominated by muons that are strongly affected by the geomagnetic field, they require a specific reconstruction procedure that differs from that used for events with zenith angles less than $60°$. The method to estimate the energy of an inclined event recorded by the SD array, described in full detail in [15], is summarised in the following.

The arrival direction (θ, ϕ) of the shower is obtained by fitting the start times of the signals recorded at the triggered stations to a plane front corrected for small time delays associated with the muon propagation as modelled in [20]. Once the shower geometry is established, the intensities of the signals are used to quantify the shower size and the impact point of the shower axis on the ground. The method is based on the observation that the shape of the muon distribution is approximately universal for a given shower direction and that only the overall normalisation of the muon distribution depends on the shower energy and primary mass [15, 21]. It has also been shown that the lateral shape of the muon density profile is consistently reproduced by different hadronic models and software packages used for air-shower simulations. These universal characteristics allow one to model the muon number density as a function of the position at the ground (muon distribution) as:

$$\rho_\mu(\vec{r}) = N_{19}\, \rho_{\mu,19}(\vec{r}; \theta, \phi). \tag{2.1}$$

Here N_{19} is a measure of the shower size and is the relative normalisation of a particular event with respect to a reference muon distribution, $\rho_{\mu,19}(\vec{r}; \theta, \phi)$ [22, 23], and $\rho_{\mu,19}$ is conventionally chosen to be the average muon density for primary protons with an energy of $10^{19}\,\text{eV}$

simulated using QGSJetII-03 [24] as the hadronic interaction model. N_{19} is thus expected to be correlated with the shower energy, and independent of the shower arrival direction. Therefore, N_{19} can be used as the energy estimator of inclined events recorded at the SD.

N_{19} is estimated by fitting the measured signals at the SD stations to the expected muon distribution for a given arrival direction, using a maximum-likelihood method based on a probabilistic model of the detector response to muon hits obtained from Geant4 [25] simulations with the $\overline{\text{Off}\underline{\text{line}}}$ framework [26] of the Pierre Auger Observatory. A residual electromagnetic component of the signal stemming from the muons themselves, mainly from decay in flight, is taken into account based on simulations (typically amounting to 20% of the muon signal) [27]. To ensure a good reconstruction, only events well-contained in the SD array are selected. This fiducial trigger requires that the reconstructed core of the shower falls within an active cell, defined as the elemental hexagon cell[1] surrounding an operational station when the six neighbouring stations in the regular hexagonal pattern are also operational, at the time of the event.

Although the actual value for N_{19} depends upon the particular choice of composition and hadronic model made for the reference distribution, the absolute energy calibration is inferred from a sub-sample of hybrid events measured simultaneously with the FD and SD that are used to calibrate the shower size N_{19} with the calorimetric shower energy measured with the FD, E_{FD}. This ensures that most of the uncertainties associated with the unknown primary composition in data and hadronic model assumed, as well as many uncertainties associated with the reconstruction, are absorbed in this robust and reliable calibration procedure based only on data.

The FD provides a nearly calorimetric, model-independent energy measurement, because the fluorescence light is produced in proportion to the electromagnetic energy deposited by the shower in the atmosphere. The longitudinal profile of the energy deposit, dE/dX, is determined from the signals at the triggered pixels of the telescope cameras after taking into account the separate fluorescence and Cherenkov light contributions, as well as light attenuation and dispersion in the atmosphere [29]. The electromagnetic energy released by the shower in the atmosphere is obtained by fitting the longitudinal profile dE/dX to a Gaisser-Hillas (GH) function [30] and integrating over the X-range. The total primary energy, E_{FD}, is then derived by adding the so-called "invisible energy" carried into the ground by high-energy muons and neutrinos, which is estimated using an unbiased and model-independent method [31]. The shower-energy estimated with the FD has a total systematic uncertainty of 14% [32].

For the calibration, only events with zenith angles greater than 60° independently triggered and reconstructed by the FD and SD are considered. The FD measurements must pass quality cuts designed to select high-quality longitudinal profiles observed under good atmospheric conditions, including the condition that the depth of the shower maximum, X_{max}, is within the field of view (FOV) of the telescopes. The latter condition together with the limited FOV of the FD may introduce a different selection efficiency for different primary masses. To avoid this effect, a strict cut on the slant depth range observed by the telescopes is also applied to ensure that the FOV is large enough to observe all plausible values of the depth of the shower maximum for the geometry of each individual shower. See [15] for a full description of the selection criteria. Finally, only events with energies above 4×10^{18} eV are accepted to ensure practically full trigger efficiency (see section 3).

---

[1]The elemental hexagon cell is the region with vertices at the barycentre of each of the six triangles around the central station, with area given by $D^2\sqrt{3}/2$ where $D = 1.5$ km is the array spacing [28].
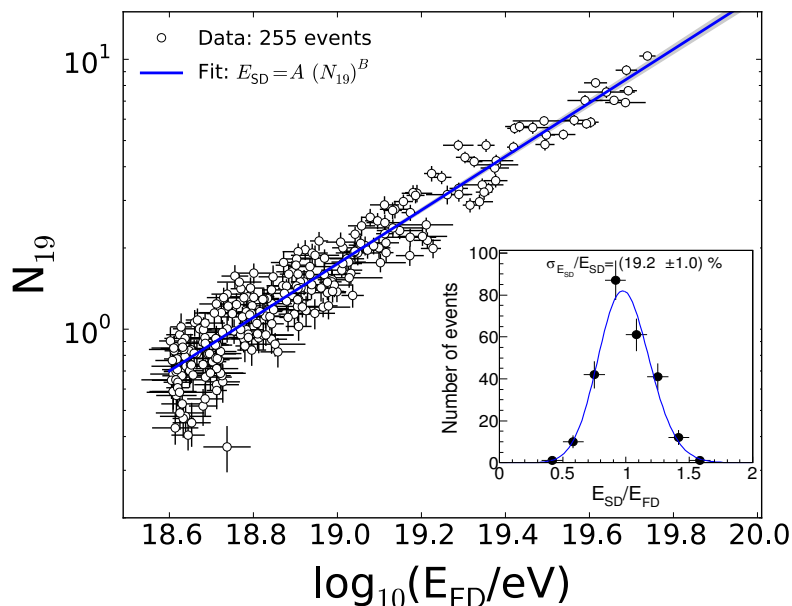
Figure 1. Correlation between the shower size parameter, N_{19}, and the reconstructed FD hybrid energy, E_{FD}, for the selected hybrid data with $\theta \geqslant 60°$ used in the fit. The uncertainties indicated by the error bars are described in the text. The solid line is the best fit of the power-law dependence $E_{SD} = A(N_{19})^B$ to the data. The corresponding ratio distribution of the SD energy E_{SD} to the FD energy E_{FD} is shown in the inset.

Here we present the calibration results using inclined events with zenith angles between $60°$ and $80°$ recorded from 1 January 2004 to 30 September 2013, increasing the data sample by about 14% with respect to the one used in previous analyses [15, 16]. A total of 255 hybrid events are selected.

The correlation between the energy estimator N_{19} and the calorimetric hybrid energy E_{FD} is well described by a simple power-law function:

$$N_{19} = A' \left(E_{FD}/10^{19}\,\text{eV} \right)^{B'}. \tag{2.2}$$

The fit is based on a tailored maximum-likelihood method [33] that includes both the uncertainties of N_{19} and E_{FD} without relying on approximations. For each event the uncertainty in N_{19} corresponds to the reconstruction uncertainty as obtained from the fit to the reference muon distribution. Shower-to-shower fluctuations of N_{19} also contribute to the spread and are taken into account. The relative uncertainty associated with shower-to-shower fluctuations is assumed to be constant in the energy range of interest and fitted to the data as an extra parameter. The uncertainty in E_{FD} assigned to each event comes from the propagation of both the statistical uncertainties of the reconstruction procedure (associated with the reconstruction of the shower geometry, the GH fit to the longitudinal profile and the correction for the invisible energy) and the uncertainties of the atmospheric parameters [32].

The resulting fit to the selected data is illustrated in figure 1. By inverting the fitted function, the SD energy estimate is given as $E_{SD} = A(N_{19})^B$ and the corresponding calibration parameters are $A = (5.701 \pm 0.086) \times 10^{18}\,\text{eV}$ and $B = 1.006 \pm 0.018$. Although statistical uncertainties of the calibration constants A and B affect the SD energy scale, their contribution is small (from 1.5% at $10^{19}\,\text{eV}$ to 4.5% at $10^{20}\,\text{eV}$), decreasing as the number of events

increase. There is also an uncertainty of $\sim 2\%$ attributed to the different angular distributions of the hybrid events and the full inclined data set used to calculate the spectrum. The main contribution to the systematic uncertainty comes from the overall systematic uncertainty of 14% from the FD energy scale. By adding the uncertainties described above in quadrature, the total systematic uncertainty in E_{SD} ranges between 14% at $10^{19}\,\mathrm{eV}$ and 17% at $10^{20}\,\mathrm{eV}$.

The resolution in E_{SD} is computed from the distribution of the ratio of $A\,(N_{19})^B/E_{\mathrm{FD}}$ for the hybrid events used for the calibration, assuming a fixed FD energy resolution of 7.6% [32] (method based on [34]). The resulting average SD energy resolution is estimated to be $(19 \pm 1)\%$ (see inset in figure 1). It is dominated by low-energy showers due to the limited number of events at the highest energies.

3 Efficiency and exposure

The final step in measuring the energy spectrum is a precise determination of the exposure for the observations. The exposure involves the time integral of the aperture, that is, the integral of the instantaneous effective area of the SD over solid angle and observation time. This integral is subsequently weighted by the trigger and event selection efficiency, which depends on the characteristics of the shower such as the nature of the primary particle, its energy and arrival direction. For low energies, the efficiency is smaller than one due to the trigger and the selection procedures (details in [15, 28]) and can in practice be a source of large uncertainty. It is thus advantageous to limit the spectral measurements to energies at which the array is fully efficient, that is, when the effective area of the SD coincides with the geometrical one.

The inclined SD data set used to measure the cosmic-ray spectrum is composed of events selected to have zenith angles between $60°$ and $80°$ and falling inside an active region of the array to guarantee that no crucial part of the shower is missing. Hence, the trigger and event selection efficiency of the SD array for inclined showers is the probability that a cosmic-ray shower reaching an active region of the array induces a trigger, is selected and finally reconstructed.

The energy for full detector efficiency is determined using hybrid events (detected with the FD and having at least one triggered SD station). To avoid biases from the primary composition, the same data selection criteria as for the energy calibration are applied (see section 2). Additionally, it is required that the shower core reconstructed with the FD technique falls within an active cell of the SD array. Assuming that the detection probabilities of the SD and FD detectors are independent, the average detection efficiency as a function of calorimetric shower energy reconstructed with the FD can be estimated from the fraction of hybrid events that trigger the SD, are selected and finally reconstructed [15]. The resulting efficiency is shown in figure 2 as a function of both shower energy E and shower size parameter N_{19}. The conversion of N_{19} to energy has been made using the calibration procedure based on data discussed in the section 2. The efficiency evaluated with the hybrid approach is subject to relatively large uncertainties, indicated as error bars, which are due largely to the limited number of events. The trigger efficiency of the SD array is found to be almost fully efficient ($>98\%$) for energies above $4\times10^{18}\,\mathrm{eV}$ or for $N_{19} > 0.7$. This value will be used as our estimate of the energy for full efficiency.

The energy for full efficiency obtained with the hybrid apprach is cross-checked using full shower and detector simulations. The sample used consists of about $20\,000$ proton showers simulated with CORSIKA [35] using QGSJetII-04 [36] with zenith angles isotropically distributed between $60°$ and $80°$ and energies ranging from $\log_{10}(E/\mathrm{eV}) = 18$ to 20, in steps
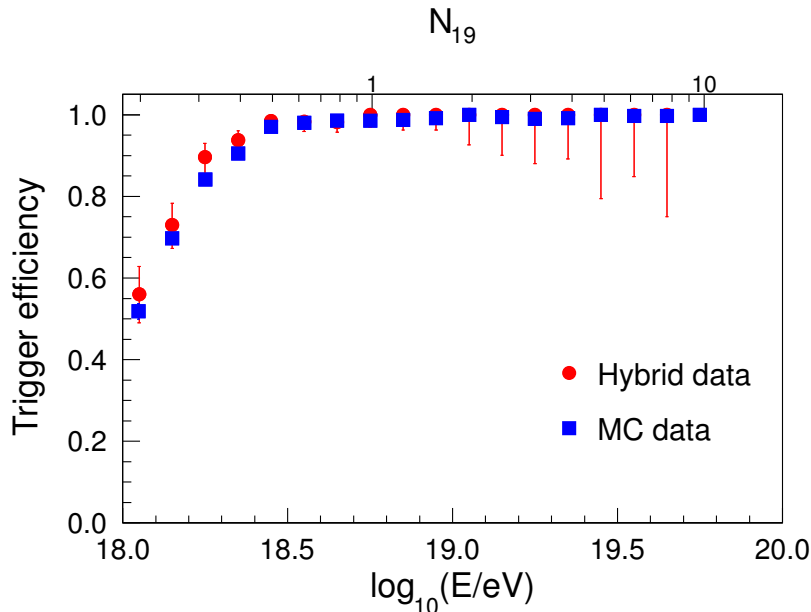
Figure 2. Trigger and event selection efficiency of the SD array for showers with zenith angles between 60° and 80° as a function of shower energy derived from the hybrid data (circles) and from the Monte Carlo simulated showers (squares). The error bars indicate the statistical uncertainty (the 68% probability contour).

of 0.5 (with a spectral index $\gamma = 1$ in each sub-interval). To generate the simulated events, these showers subsequently underwent a full simulation of the detector response, within the $\overline{\text{Off}\underline{\text{line}}}$ framework, with random impact points in the SD array. Only showers with impact points in an active region of the array are considered for this analysis. For each event, the full trigger and event selection chain are applied.

The trigger efficiency for inclined showers depends mainly on the total number of muons at the ground for a given arrival direction, which is proportional to the reconstructed shower size parameter N_{19}. A recent study [16] has reported that the measured muon number in inclined showers at ground level exceeds expectations obtained with simulations and various hadronic interaction models (even when assuming a pure iron composition). This implies that simulations and data have a different $N_{19}-E$ correlation, that is, the MC energy is not directly comparable to E_{FD} for the same muon content. To carry out a comparison between using hybrid data and simulations, we correct for the muon deficit observed in simulations by converting the shower size of each simulated event into energy using the same calibration procedure applied for the data. The resulting efficiency as a function of both shower energy and shower size parameter is also shown in figure 2. The trigger and selection become almost fully efficient at energies above 4×10^{18} eV in agreement with hybrid data. It has been tested with simulations that above this energy, the detector is fully efficient independently of the particular choice of mass composition and hadronic model.

The choice of a fiducial trigger based on active hexagons allows us to exploit the regularity of the array [28]. The geometrical aperture of the array is obtained as a multiple of the aperture of an elemental hexagon cell. Above the energy for full efficiency, the detection area per cell is $1.95 \, \text{km}^2$, which results in an aperture of $a_{\text{cell}} = 1.35 \, \text{km}^2$ sr for showers with zenith angles between 60° and 80°. The calculation of the integrated exposure over a given period

of time simply amounts to counting the operational cells as a function of time, $N_{\text{cell}}(t)$, and integrating the corresponding aperture, $N_{\text{cell}}(t) \times a_{\text{cell}}$, over time. The overall uncertainty on the integrated exposure is less than 3% [28].

In January 2004 the initial area spanned by the array was about $34\,\text{km}^2$ and it rose steadily until August 2008 when over 1600 surface detectors were in operation. The calculation of the surface area is the same as that used for the spectrum measured with events at zenith angles less than $60°$ and has been done numerically, making use of the trigger rate at each station [28]. The integrated exposure for showers with zenith angles between $60°$ and $80°$ amounts to $(10\,890 \pm 330)\,\text{km}^2\,\text{sr}\,\text{yr}$ in the time period from 1 January 2004 to 31 December 2013 (which corresponds to 29% of the exposure for showers with $\theta < 60°$ in the same period). This calculation excludes periods during which the array was not sufficiently stable, which add up to a small fraction of the total time (of the order of 5%).

4   Spectrum

Inclined events recorded by the SD in the time period between 1 January 2004 and 31 December 2013 were analysed and calibrated with the procedure outlined above. The resulting data set consists of 254 686 events that fell on the active part of the array with zenith angles in the interval between $60°$ and $80°$. To avoid large uncertainties due to the trigger and event selection efficiencies, only events having energies greater than $4 \times 10^{18}\,\text{eV}$ are considered for the spectrum calculation, reducing the sample to 15 614 events.

The differential flux of cosmic rays at a certain energy E, $J(E)$, is obtained by dividing the energy distribution of the cosmic rays by the accumulated exposure in the corresponding zenith-angle interval for the energies in the range of full trigger efficiency. Figure 3 shows this ratio for the selected events (also displayed as a function of the equivalent shower size N_{19}). This is a raw distribution since effects of the finite resolution of the SD energy measurement have not yet been taken into account. Note that this figure also shows the ratio below $4 \times 10^{18}\,\text{eV}$ where it is not expected that the flux will be reproduced accurately because of the energy dependence of the triggering efficiency (see figure 2).

A correction must be applied to account for the effect of the resolution in the energy determination, responsible for a bin-to-bin event migration. The number of events in a given bin is contaminated by movements of reconstructed energies from the adjacent bins. For an energy spectrum which is steeply falling, upward fluctuations into a given bin are not completely compensated by other fluctuations from the other direction, and the net effect is an overestimate of the flux when this correction is not applied. Due to this, the measured spectrum is shifted towards higher energies with respect to the true spectrum. To correct for this, a forward-folding approach is applied. Monte Carlo simulations are used to determine the resolution of the SD energy estimator based on the shower size parameter, N_{19}, for different assumptions on the primary mass and hadronic interaction models. Then the average resolution is converted to the SD energy resolution using the same energy scale as obtained from the data. In addition, intrinsic fluctuations (also called shower-to-shower fluctuations) contribute to the bin migration. In this case, these fluctuations are modelled with a normal distribution that has a constant relative standard deviation, $\sigma(N_{19})/N_{19}$, and are estimated in the data-calibration procedure as explained in [15], resulting in $\sigma(N_{19})/N_{19} = (14 \pm 1)\%$. From the SD energy resolution and intrinsic fluctuations, a bin-to-bin migration matrix is derived. The matrix is then used to find a flux parameterisation that matches the measured data when forward-folded.
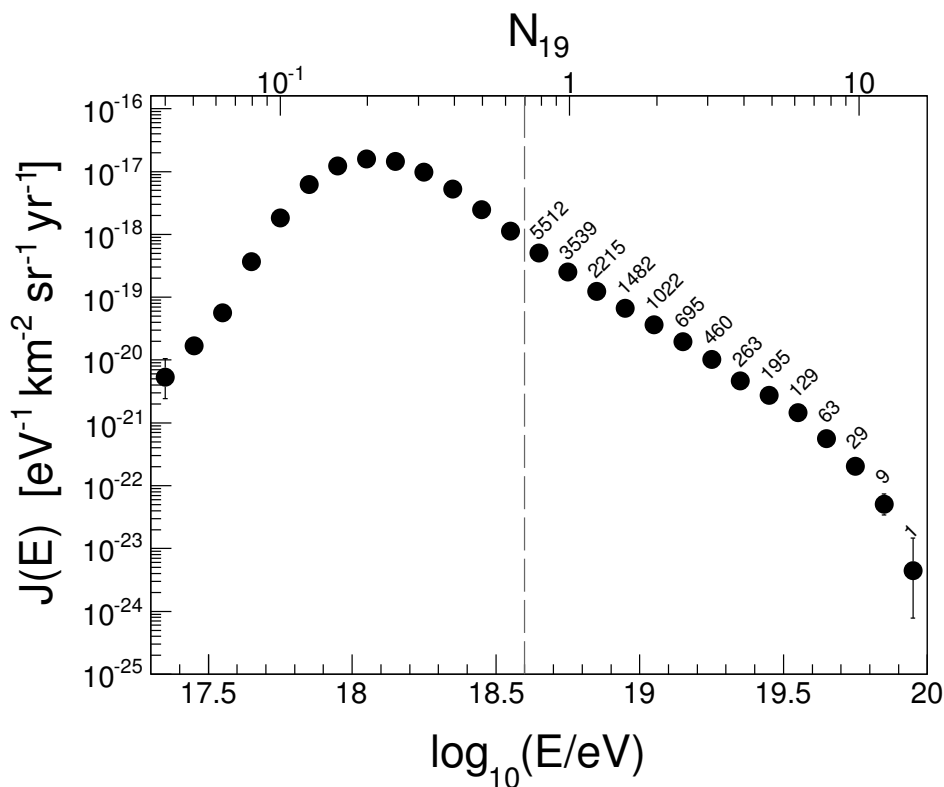
Figure 3. Uncorrected energy spectrum of the cosmic rays derived from inclined events with zenith angles $60° \leqslant \theta \leqslant 80°$ in terms of energy and shower size. Only statistical uncertainties are shown. The number of events in each of the bins above $4{\times}10^{18}$ eV (vertical dashed line) is given above the points.
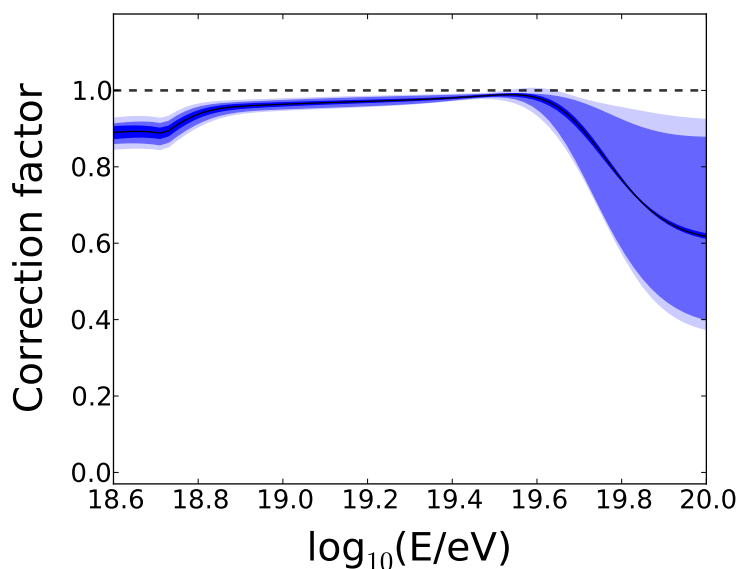

Figure 4. Correction factor applied to the measured spectrum to account for the detector effects as a function of the cosmic-ray energy. The uncertainty due to the energy resolution is shown with the dark band, and that due to shower-to-shower fluctuations with the blue band. The total uncertainty, also including the uncertainty of the fit, is shown by the light band.

We assume a common parameterisation for the spectrum given a power law below the ankle and a power law plus a smoothly changing function above,

$$J(E) \propto E^{-\gamma_1} \qquad\qquad\qquad ; E < E_{\mathrm{ankle}}, \qquad\qquad (4.1)$$

$$J(E) \propto E^{-\gamma_2} \left[1 + \left(\frac{E}{E_{\mathrm{s}}} \right)^{\Delta\gamma} \right]^{-1} \qquad ; E \geqslant E_{\mathrm{ankle}}, \qquad\qquad (4.2)$$

where E_{s} is the energy at which the flux falls to one-half of the value of the power-law extrapolation of the intermediate region and $\Delta\gamma$ gives the increment of the spectral index beyond the suppression region.[2] This parameterisation was convolved with the migration matrix and the resulting flux was fitted to the measured spectrum, using a binned maximum-likelihood approach assuming Poisson statistics. As E_{ankle} is very close to the saturation energy for inclined showers, neither E_{ankle} nor γ_1 can be reliably established from the data. These parameters are relevant for the unfolding of the lower-energy part of the spectrum. They were fixed to the values obtained in the spectrum reported in [9], $\gamma_1 = 3.23 \pm 0.01 \pm 0.07\,\mathrm{(sys)}$ and $E_{\mathrm{ankle}} = (5.25 \pm 0.12 \pm 0.24\,\mathrm{(sys)}) \times 10^{18}\,\mathrm{eV}$, while the other parameters were left free. The convolved flux is finally divided by the input flux to obtain the correction factors which are in turn applied to the measured binned spectrum.

The correction factor resulting from the fit of the assumed parameterisation is shown in figure 4. The uncertainty from the fit was obtained by propagating the covariance matrix of the fitted parameters into the correction function. A systematic uncertainty is attributed to possible variations of the shower-to-shower fluctuations, which can arise if the mass component changes and because of the changing X_{max} over the energy range of interest. Although recent results [16] favour a transition from lighter to heavier elements in the energy range considered, here we assume a conservative scenario where the relative fluctuations are allowed to vary between 4% (corresponding to a pure iron composition) and 21% (corresponding to a pure proton composition) over the full energy range. Finally, the propagated uncertainty in the average resolution of the energy estimator N_{19}, estimated to be on the order of 10%, was also included. The uncertainty in the correction factor that arises from the uncertainties in the ankle parameters (E_{ankle} and γ_1), fixed to the values reported in [9], is negligible (<1% below E_{s}). In figure 4, in addition to the total uncertainty (light band), the last two uncertainty components are shown separately to illustrate that the main contribution is the systematic uncertainty due to variations of the shower-to-shower fluctuations.

The spectrum, corrected for energy resolution, is shown in figure 5. The error bars represent statistical uncertainties only. The flux is multiplied by E^3 to better present its features, a flat region above $4 \times 10^{18}\,\mathrm{eV}$ up to the steepening at energies above about $4 \times 10^{19}\,\mathrm{eV}$. The light shaded boxes indicate the total systematic uncertainties (less than $\sim$40% up to $4 \times 10^{19}\,\mathrm{eV}$, and then increasing up to $\sim$200% for the highest energy bin), which include the uncertainty in the calibration parameters propagated to the flux, a global uncertainty derived from the SD exposure calculation (3%), the uncertainty arising from the unfolding process, and the global systematic uncertainty of the FD energy scale (14%) from the hybrid-calibration procedure. In figure 6 these separate contributions to the systematic uncertainties in the derived flux are shown as a function of the cosmic-ray energy.

---

[2]Note that $\Delta\gamma = 1/\ln(W_{\mathrm{c}})$ in the equivalent expression used in [8], where W_{c} defines the width of the transition region at the suppression.
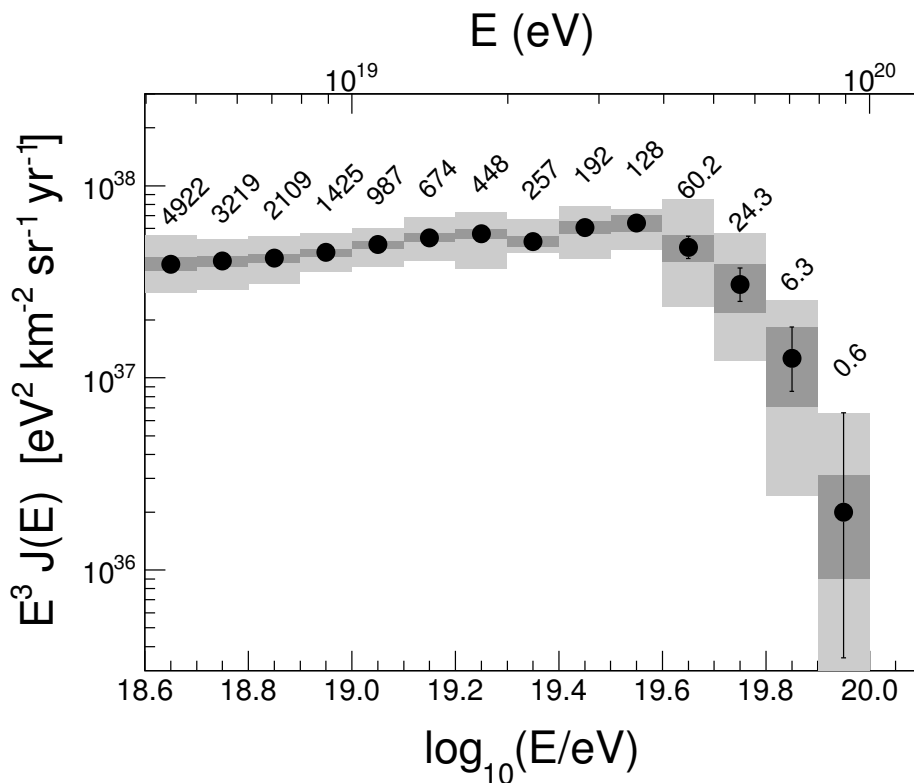
Figure 5. Energy spectrum of the cosmic rays, corrected for energy resolution, derived from inclined data with zenith angles $60° \leqslant \theta \leqslant 80°$. The error bars represent statistical uncertainties. The light shaded boxes indicate the total systematic uncertainties. For illustration purposes, the systematic uncertainties excluding the uncertainty from the energy scale are also shown as darker boxes. The effective number of events, after correcting the flux for energy resolution, is given above the points.

5 Discussion

The characteristic features of the spectrum have been quantified by fitting the model given by eqs. (4.1) and (4.2), which assumes a spectrum with a sharp ankle and a smooth suppression at the highest energies, to the unfolded spectrum. The result of the best fit is shown as a solid line in figure 7. Another approach is to describe the spectrum with three power laws separated by two breaking points as illustrated by a dashed line in figure 7. The first model improves marginally the description of the abrupt change of slope observed at higher energies. The spectral parameters from the best fits to the data are given in table 1, quoting both statistical and systematic uncertainties.

Note that, as explained above, the selected energy threshold of 4×10^{18} eV is, by coincidence, close to the value obtained for the ankle, $(5.25 \pm 0.12)\times10^{18}$ eV, in the combined analysis of hybrid events and SD events [9]. It is thus not possible to analyse the ankle transition properly. Nevertheless, the raw data do clearly display such a feature (see figure 3) which we do not analyse any further here due to the large uncertainty in the efficiency in this region (see figure 2). As a consequence, the γ_1 and E_{ankle} parameters in equation (4.1) have been fixed to the values reported in [9].

Both models consistently describe the "flat" region of the spectrum above the ankle up to the observed onset of the suppression at $\sim4\times10^{19}$ eV by a power law with a spectral index
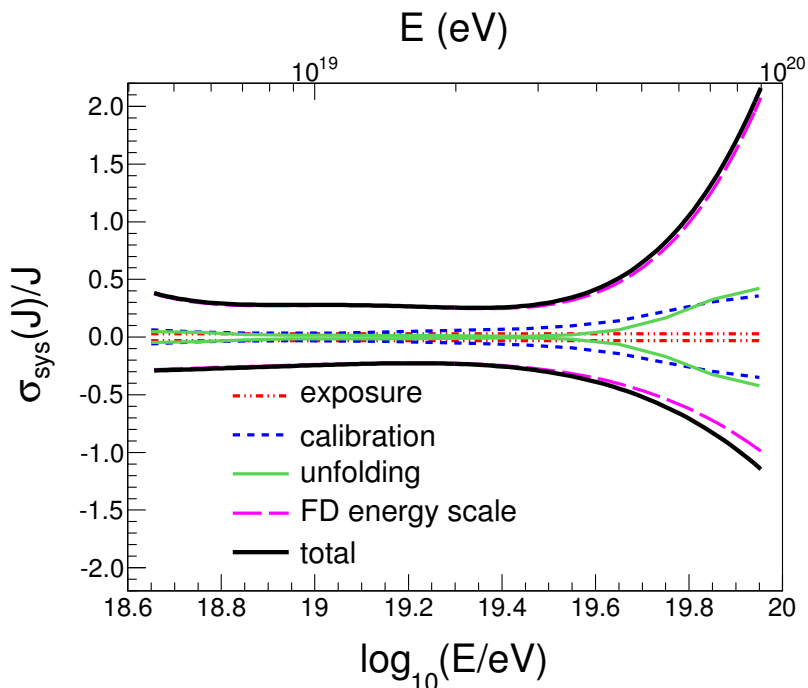
Figure 6. Systematic uncertainties in the derived flux as a function of the cosmic-ray energy. For a description of the different sources of systematic uncertainty, see the text.

Parameter	Power laws	Power laws + smooth suppression
$\gamma_2 (E > E_{\text{ankle}})$	$2.71 \pm 0.02 \pm 0.1 \, (\text{sys})$	$2.70 \pm 0.02 \pm 0.1 \, (\text{sys})$
E_{break}	$(4.01 \pm 0.21^{+1.0}_{-1.7} \, (\text{sys})) \times 10^{19} \, \text{eV}$	
$\gamma_3 (E > E_{\text{break}})$	$5.98 \pm 0.61^{+0.9}_{-1.4} \, (\text{sys})$	
E_{s}		$(5.12 \pm 0.25^{+1.0}_{-1.2} \, (\text{sys})) \times 10^{19} \, \text{eV}$
$\Delta\gamma$		$5.4 \pm 1.0^{+2.1}_{-1.1} \, (\text{sys})$
χ^2/ndof	$15.7/10$	$13.2/10$

Table 1. Fitted parameters, with statistical and systematic uncertainties, parameterising the energy spectrum measured with the inclined events.

of $\gamma_2 = 2.7$. The spectral index after the steepening is less certain due to the low number of events and large systematic uncertainties. The significance of the suppression[3] is $\sim 6.6\,\sigma$ with 220.4 events expected above the break energy E_{break} while only 102 events were observed.

A different observable that characterises the suppression is the energy $E_{1/2}$ at which the integral spectrum drops by a factor of two relative to the power-law extrapolation from lower energies, as suggested in [38]. Here, the integral spectrum was computed by integrating the parameterisation given by eqs. (4.1) and (4.2) and the parameters reported in table 1. The result yields $E_{1/2} = (3.21 \pm 0.01 \pm 0.8 \, (\text{sys})) \times 10^{19} \, \text{eV}$, which is smaller than the value of $\approx 5.3 \times 10^{19} \, \text{eV}$ predicted for the GZK energy cutoff of protons [38] (practically independent of the generation index of the assumed energy spectrum), with a difference at the level of

---

[3]Following the recipe given in [37], the null hypothesis that the power law with spectral index $\gamma_2 = 2.71 \pm 0.02$ continues beyond the suppression point can be rejected due to the low probability $(5^{+3}_{-2}) \times 10^{-11}$.
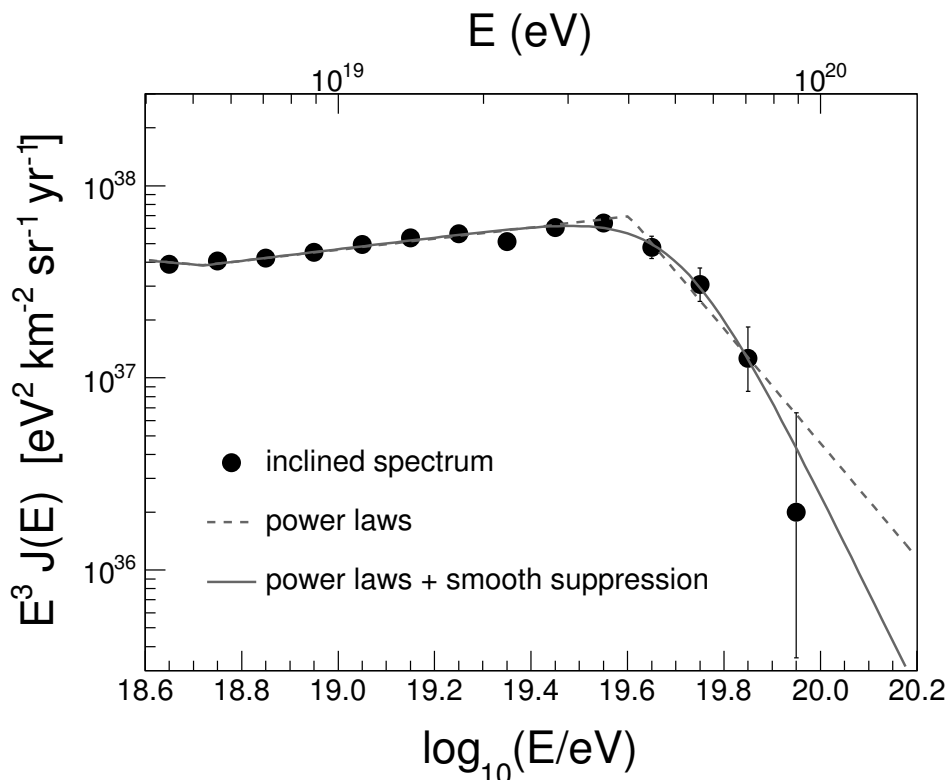
Figure 7. Energy spectrum of the cosmic rays, corrected for energy resolution, derived from inclined data fitted with simple power laws (dashed line) and with eqs. (4.1) and (4.2) (solid line). The systematic uncertainty on the energy scale is 14%.

$2.6\,\sigma$. In [38] the assumption was made that the sources of ultra-high energy cosmic rays are uniformly distributed over the universe and are accelerators of protons. In reality, sources are discrete and in the GZK region the shape of the spectrum will be dominated by the actual distribution of sources around us. Further discussion of this point is given in [39]. Other scenarios for the high-energy suppression of the spectrum (e.g., [40–43]) attribute it to the limiting acceleration energy at the sources rather than to the GZK effect, providing a good description of the combined Auger energy spectrum as shown in [44].

To compare the spectrum obtained here with other measurements, we have adopted the technique suggested in [45] in which the differential flux at each energy is compared with the expected differential flux from a reference spectrum. We choose as reference a spectrum with an index[4] of 2.67 fitted to the flux presented here (see figure 5) in the energy bin corresponding to $\log_{10}(E/\text{eV}) = 18.95$ (bin width of 0.1), which contains over 1425 events. The reference spectrum is thus

$$J_{\text{exp}} = 2.52 \times 10^{31}\,(E/\text{eV})^{-2.67}\,\text{eV}^{-1}\,\text{km}^{-2}\,\text{sr}^{-1}\,\text{yr}^{-1}. \tag{5.1}$$

In figure 8 the spectrum obtained with inclined events is displayed as a fractional difference (also called the residual) with respect to the reference spectrum, in comparison to the residual for the spectrum obtained from data with zenith angles less than 60° [9]. The comparison shows that both spectra are in agreement within errors. We note that the last two

---

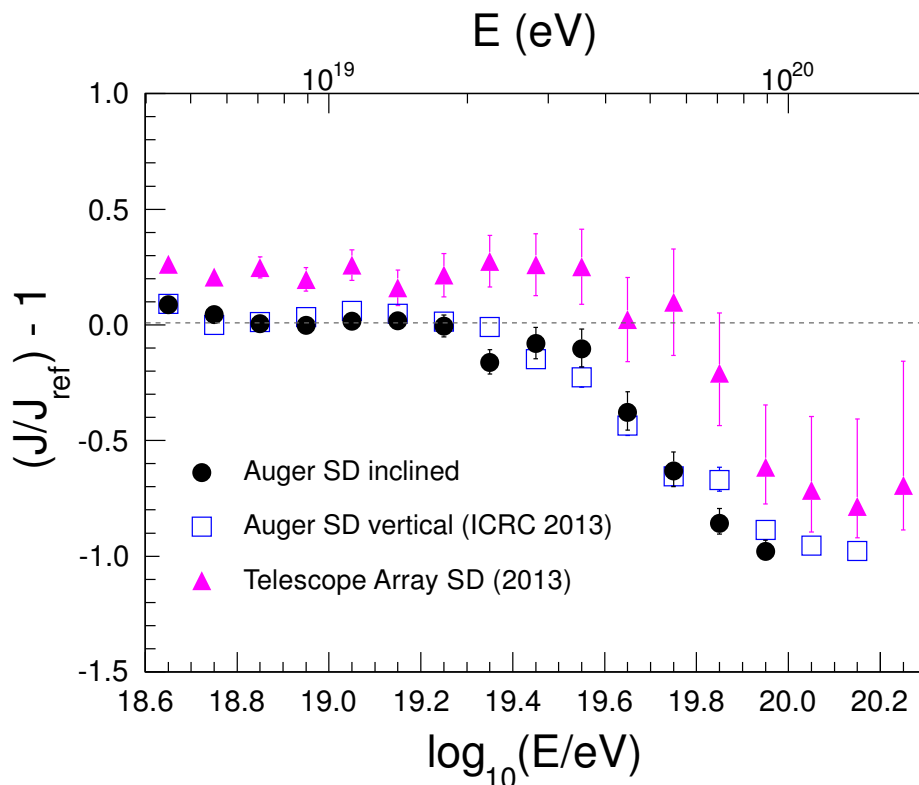[4]The index of the reference spectrum has no physical significance, so its choice is quite arbitrary.

Figure 8. Fractional difference between the energy spectrum of cosmic rays derived from SD data with $\theta \geqslant 60°$ recorded at the Pierre Auger Observatory and a reference spectrum with an index of 2.67. Residuals for spectra derived from Auger SD data with $\theta < 60°$ [9] and the Telescope Array SD data with $\theta < 55°$ [12] are also shown for comparison.

points are systematically below the corresponding measurement obtained for Auger events with zenith angles less than 60°. Also the point corresponding to $\log_{10}(E/\text{eV}) = 19.35$ is below the vertical one. However, the differences are at the $2\,\sigma$ level.

Figure 8 also displays the spectrum obtained from SD events with zenith angles less than 55° recorded with the Telescope Array (TA) detector [12]. The comparison of the residuals for the three spectra (also illustrated in the form of $J\,E^3$ in figure 9) shows that in the region between the ankle and the suppression the Auger spectra fit well due to our choice of reference spectrum, and the average of the residuals for TA is about $+23\%$. The spectra determined by the Auger and TA Observatories are consistent in normalisation and shape within the systematic uncertainties in the energy scale quoted by the two collaborations [46]. However, differences are clearly seen in the high-energy region and are not understood thus far. Understanding the origin of this difference, whether from anisotropies at high energies, composition-related effects, experimental issues or any other reason, is of high priority in the efforts to understand the origin of the UHECRs. However the dedicated study of this discrepancy is beyond the scope of this work. Since 2012 there has been a collaborative effort between the Pierre Auger and Telescope Array Collaborations to investigate the level of agreement between the different measurements of the UHECR energy spectrum and to understand the sources of possible discrepancies, by examining the different measurement techniques and analysis methods employed by these groups. The latest results obtained by the energy spectrum working group can be found in [46].
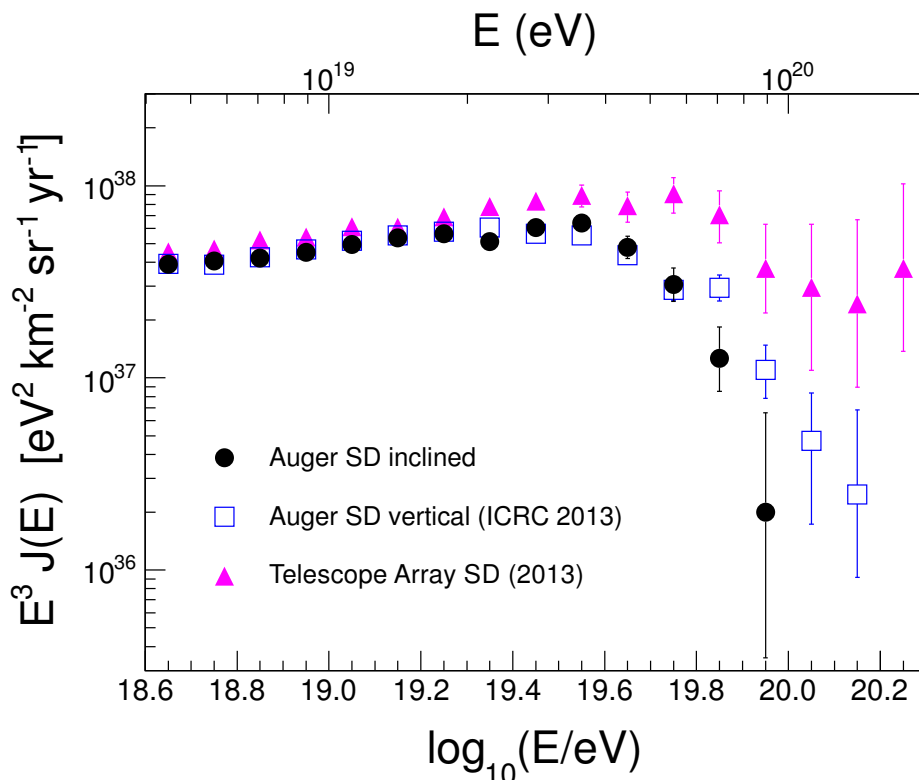
Figure 9. Compilation of the energy spectrum of cosmic rays derived from SD data recorded at the Pierre Auger Observatory with $\theta \geqslant 60°$ (circles) and $\theta < 60°$ (squares), and at the Telescope Array with $\theta < 55°$ (triangles).

6 Summary

The cosmic-ray spectrum has been obtained for energies exceeding 4×10^{18} eV using showers with zenith angles between 60° and 80° recorded with the surface detector of the Pierre Auger Observatory during the time period between 1 January 2004 and 31 December 2013. It has been shown that the SD array becomes fully efficient for inclined events above this energy. The results can be described by a power-law spectrum with spectral index 2.7 above 5×10^{18} eV and clearly indicate a steepening of the cosmic-ray spectrum above an energy around 4×10^{19} eV. These features and the normalisation of the spectrum are in agreement with previous measurements made with the Pierre Auger Observatory (using SD data and hybrid data with zenith angles less than 60°) and also with the measurements of the Telescope Array.

The inclined data set is independent and complementary to the vertical data set and its reconstruction is performed using an independent method. These data provide a 29% increase in number of events over the previous event set. In addition to obtaining an independent measurement of the cosmic-ray spectrum reported here, the inclined data are being analysed to explore primary composition, to constrain the current models that attempt to describe the hadronic interactions at energies above 4×10^{18} eV ($E_{CM} \approx 87$ TeV), and to improve the studies of the arrival directions of the cosmic rays by extending the accessible fraction of the sky to 85%.

References

[1] PIERRE AUGER collaboration, J. Abraham et al., *Properties and performance of the prototype instrument for the Pierre Auger Observatory*, *Nucl. Instrum. Meth.* **A 523** (2004) 50 [INSPIRE].

[2] PIERRE AUGER collaboration, A. Aab et al., *The Pierre Auger cosmic ray observatory*, accepted for publication in *Nucl. Instrum. Meth.* (2015) [arXiv:1502.01323] [INSPIRE].

[3] PIERRE AUGER collaboration, J. Abraham et al., *The fluorescence detector of the Pierre Auger Observatory*, *Nucl. Instrum. Meth.* **A 620** (2010) 227 [arXiv:0907.4282] [INSPIRE].

[4] PIERRE AUGER collaboration, J. Abraham et al., *Observation of the suppression of the flux of cosmic rays above* 4×10^{19} *eV*, *Phys. Rev. Lett.* **101** (2008) 061101 [arXiv:0806.4302] [INSPIRE].

[5] K. Greisen, *End to the cosmic ray spectrum?*, *Phys. Rev. Lett.* **16** (1966) 748 [INSPIRE].

[6] G.T. Zatsepin and V.A. Kuzmin, *Upper limit of the spectrum of cosmic rays*, *JETP Lett.* **4** (1966) 78 [*Pisma Zh. Eksp. Teor. Fiz.* **4** (1966) 114] [INSPIRE].

[7] HiRes collaboration, R.U. Abbasi et al., *First observation of the Greisen-Zatsepin-Kuzmin suppression*, *Phys. Rev. Lett.* **100** (2008) 101101 [astro-ph/0703099] [INSPIRE].

[8] PIERRE AUGER collaboration, J. Abraham et al., *Measurement of the energy spectrum of cosmic rays above* 10^{18} *eV using the Pierre Auger Observatory*, *Phys. Lett.* **B 685** (2010) 239 [arXiv:1002.1975] [INSPIRE].

[9] PIERRE AUGER collaboration, A. Schulz, *The measurement of the energy spectrum of cosmic rays above* 3×10^{17} *eV with the Pierre Auger Observatory*, in *Contributions to the* 33$^{\rm rd}$ *International Cosmic Ray Conference (ICRC* 2013*)*, Rio de Janeiro Brazil (2013) [arXiv:1307.5059] [INSPIRE].

[10] TELESCOPE ARRAY collaboration, T. Abu-Zayyad et al., *The surface detector array of the Telescope Array experiment*, *Nucl. Instrum. Meth.* **A 689** (2012) 87 [arXiv:1201.4964] [INSPIRE].

[11] H. Tokuno et al., *New air fluorescence detectors employed in the Telescope Array experiment*, *Nucl. Instrum. Meth.* **A 676** (2012) 54 [arXiv:1201.0002] [INSPIRE].

[12] TELESCOPE ARRAY collaboration, T. Abu-Zayyad et al., *The cosmic ray energy spectrum observed with the surface detector of the Telescope Array experiment*, *Astrophys. J.* **768** (2013) L1 [arXiv:1205.5067] [INSPIRE].

[13] A.M. Hillas, J.D. Hollows, H.W. Hunter and D.J. Marsden, *Calculations on the particle and energy-loss densities in extensive air showers at large axial distances*, in *Proceedings of the* 11$^{\rm th}$ *Int. Cosmic Ray Conf.*, Budapest Hungary (1969) [*Acta Phys. Acad. Sci. Hung.* **29** (1970) 533] [INSPIRE].

[14] M. Ave, R.A. Vazquez, E. Zas, J.A. Hinton and A.A. Watson, *The rate of cosmic ray showers at large zenith angles: a step towards the detection of ultrahigh-energy neutrinos by the Pierre Auger Observatory*, *Astropart. Phys.* **14** (2000) 109 [astro-ph/0003011] [INSPIRE].

[15] PIERRE AUGER collaboration, A. Aab et al., *Reconstruction of inclined air showers detected with the Pierre Auger Observatory*, *JCAP* **08** (2014) 019 [arXiv:1407.3214] [INSPIRE].

[16] PIERRE AUGER collaboration, A. Aab et al., *Muons in air showers at the Pierre Auger Observatory: mean number in highly inclined events*, *Phys. Rev.* **D 91** (2015) 032003 [*Erratum ibid.* **D 91** (2015) 059901] [arXiv:1408.1421] [INSPIRE].

[17] PIERRE AUGER collaboration, A. Aab et al., *Searches for anisotropies in the arrival directions of the highest energy cosmic rays detected by the Pierre Auger Observatory*, *Astrophys. J.* **804** (2015) 15 [arXiv:1411.6111] [INSPIRE].

[18] PIERRE AUGER collaboration, A. Aab et al., *Large scale distribution of ultra high energy cosmic rays detected at the Pierre Auger Observatory with zenith angles up to 80°*, *Astrophys. J.* **802** (2015) 111 [arXiv:1411.6953] [INSPIRE].

[19] K.S. Capelle, J.W. Cronin, G. Parente and E. Zas, *On the detection of ultrahigh-energy neutrinos with the Auger Observatory*, *Astropart. Phys.* **8** (1998) 321 [astro-ph/9801313] [INSPIRE].

[20] L. Cazon, R.A. Vazquez, A.A. Watson and E. Zas, *Time structure of muonic showers*, *Astropart. Phys.* **21** (2004) 71 [astro-ph/0311223] [INSPIRE].

[21] M. Ave, J.A. Hinton, R.A. Vazquez, A.A. Watson and E. Zas, *Constraints on the ultrahigh-energy photon flux using inclined showers from the Haverah Park array*, *Phys. Rev.* **D 65** (2002) 063007 [astro-ph/0110613] [INSPIRE].

[22] M. Ave, R.A. Vazquez and E. Zas, *Modeling horizontal air showers induced by cosmic rays*, *Astropart. Phys.* **14** (2000) 91 [astro-ph/0011490] [INSPIRE].

[23] H.P. Dembinski, P. Billoir, O. Deligny and T. Hebbeker, *A phenomenological model of the muon density profile on the ground of very inclined air showers*, *Astropart. Phys.* **34** (2010) 128 [arXiv:0904.2372] [INSPIRE].

[24] S. Ostapchenko, *Non-linear screening effects in high energy hadronic interactions*, *Phys. Rev.* **D 74** (2006) 014026 [hep-ph/0505259] [INSPIRE].

[25] GEANT4 collaboration, J. Allison et al., *GEANT4 developments and applications*, *IEEE Trans. Nucl. Sci.* **53** (2006) 270 [INSPIRE].

[26] S. Argiro et al., *The offline software framework of the Pierre Auger Observatory*, *Nucl. Instrum. Meth.* **A 580** (2007) 1485 [arXiv:0707.1652] [INSPIRE].

[27] I. Valino, J. Alvarez-Muniz, M. Roth, R.A. Vazquez and E. Zas, *Characterisation of the electromagnetic component in ultra-high energy inclined air showers*, *Astropart. Phys.* **32** (2010) 304 [arXiv:0910.2873] [INSPIRE].

[28] PIERRE AUGER collaboration, J. Abraham et al., *Trigger and aperture of the surface detector array of the Pierre Auger Observatory*, *Nucl. Instrum. Meth.* **A 613** (2010) 29 [arXiv:1111.6764] [INSPIRE].

[29] M. Unger, B.R. Dawson, R. Engel, F. Schussler and R. Ulrich, *Reconstruction of longitudinal profiles of ultra-high energy cosmic ray showers from fluorescence and Cherenkov light measurements*, *Nucl. Instrum. Meth.* **A 588** (2008) 433 [arXiv:0801.4309] [INSPIRE].

[30] T.K. Gaisser and A.M. Hillas, *Reliability of the method of constant intensity cuts for reconstructing the average development of vertical showers*, in *Proceedings of the* 15th *ICRC*, **8**, Plotdiv Bulgaria (1977), pg. 353.

[31] PIERRE AUGER collaboration, M. Tueros, *Estimate of the non-calorimetric energy of showers observed with the fluorescence and surface detectors of the Pierre Auger Observatory*, in *Proceedings of the* 33rd *Int. Cosmic Ray Conf.*, Rio de Janeiro Brazil (2013) [arXiv:1307.5059] [INSPIRE].

[32] PIERRE AUGER collaboration, V. Verzi, *The energy scale of the Pierre Auger Observatory*, in *Proceedings of the* 33rd *Int. Cosmic Ray Conf.*, Rio de Janeiro Brazil (2013) [arXiv:1307.5059] [INSPIRE].

[33] H.P. Dembinski, B. Kégl, I.C. Mariş, M. Roth and D. Veberič, *A likelihood method to cross-calibrate air-shower detectors*, arXiv:1503.09027 [INSPIRE].

[34] R.C. Geary, *The frequency distribution of the quotient of two normal variates*, *J. Roy. Stat. Soc.* **93** (1930) 442.

[35] D. Heck, G. Schatz, T. Thouw, J. Knapp and J.N. Capdevielle, *CORSIKA: a Monte Carlo code to simulate extensive air showers*, report FZKA-6019, Forschungszentrum Karlsruhe, Karlsruhe Germany (1998) [ɪɴSPIRE].

[36] S. Ostapchenko, *Monte Carlo treatment of hadronic interactions in enhanced Pomeron scheme: I. QGSJET-II model*, *Phys. Rev.* **D 83** (2011) 014018 [arXiv:1010.1869] [ɪɴSPIRE].

[37] J.D. Hague, B.R. Becker, M.S. Gold and J.A.J. Matthews, *Power laws and the cosmic ray energy spectrum*, *Astropart. Phys.* **27** (2007) 455 [astro-ph/0610865] [ɪɴSPIRE].

[38] V. Berezinsky, A.Z. Gazizov and S.I. Grigorieva, *On astrophysical solution to ultrahigh-energy cosmic rays*, *Phys. Rev.* **D 74** (2006) 043005 [hep-ph/0204357] [ɪɴSPIRE].

[39] M. Ahlers, L.A. Anchordoqui and A.M. Taylor, *Ensemble fluctuations of the flux and nuclear composition of ultrahigh energy cosmic ray nuclei*, *Phys. Rev.* **D 87** (2013) 023004 [arXiv:1209.5427] [ɪɴSPIRE].

[40] R. Aloisio, V. Berezinsky and A. Gazizov, *Ultra high energy cosmic rays: the disappointing model*, *Astropart. Phys.* **34** (2011) 620 [arXiv:0907.5194] [ɪɴSPIRE].

[41] D. Allard, *Extragalactic propagation of ultrahigh energy cosmic-rays*, *Astropart. Phys.* **39-40** (2012) 33 [arXiv:1111.3290] [ɪɴSPIRE].

[42] P.L. Biermann and V. de Souza, *Centaurus A: the one extragalactic source of cosmic rays with energies above the knee*, *Astrophys. J.* **746** (2012) 72 [arXiv:1106.0625] [ɪɴSPIRE].

[43] A.M. Taylor, *UHECR composition models*, *Astropart. Phys.* **54** (2014) 48 [arXiv:1401.0199] [ɪɴSPIRE].

[44] K.-H. Kampert and P. Tinyakov, *Cosmic rays from the ankle to the cutoff*, *Comptes Rendus Physique* **15** (2014) 318 [arXiv:1405.0575] [ɪɴSPIRE].

[45] A.A. Watson, *High-energy cosmic rays and the Greisen-Zatsepin-Kuz'min effect*, *Rept. Prog. Phys.* **77** (2014) 036901 [arXiv:1310.0325] [ɪɴSPIRE].

[46] Pierre Auger and Telescope Array collaborations, I.C. Mariş et al., *The energy spectrum of ultra high energy cosmic rays*, in *Proceedings of the International Symposium UHECR2014*, in preparation, Springdale U.S.A. (2014).

The Pierre Auger collaboration

A. Aab[41], P. Abreu[65], M. Aglietta[52], E.J. Ahn[82], I. Al Samarai[28], I.F.M. Albuquerque[16],
I. Allekotte[1], P. Allison[87], A. Almela[11, 8], J. Alvarez Castillo[58], J. Alvarez-Muñiz[75], R. Alves
Batista[40], M. Ambrosio[43], A. Aminaei[59], L. Anchordoqui[81], S. Andringa[65], C. Aramo[43],
V.M. Aranda [72], F. Arqueros[72], N. Arsene[68], H. Asorey[1, 24], P. Assis[65], J. Aublin[30], M. Ave[1],
M. Avenier[31], G. Avila[10], N. Awal[85], A.M. Badescu[69], K.B. Barber[12], J. Bäuml[35], C. Baus[35],
J.J. Beatty[87], K.H. Becker[34], J.A. Bellido[12], C. Berat[31], M.E. Bertaina[52], X. Bertou[1],
P.L. Biermann[38], P. Billoir[30], S.G. Blaess[12], A. Blanco[65], M. Blanco[30], C. Bleve[47], H. Blümer[35, 36],
M. Boháčová[26], D. Boncioli[51], C. Bonifazi[22], N. Borodai[63], J. Brack[79], I. Brancus[66],
A. Bridgeman[36], P. Brogueira[65], W.C. Brown[80], P. Buchholz[41], A. Bueno[74], S. Buitink[59],
M. Buscemi[43], K.S. Caballero-Mora[56], B. Caccianiga[42], L. Caccianiga[30], M. Candusso[44],
L. Caramete[67], R. Caruso[45], A. Castellina[52], G. Cataldi[47], L. Cazon[65], R. Cester[46], A.G. Chavez[57],
A. Chiavassa[52], J.A. Chinellato[17], J. Chudoba[26], M. Cilmo[43], R.W. Clay[12], G. Cocciolo[47],
R. Colalillo[43], A. Coleman[88], L. Collica[42], M.R. Coluccia[47], R. Conceição[65], F. Contreras[9],
M.J. Cooper[12], A. Cordier[29], S. Coutu[88], C.E. Covault[77], J. Cronin[89], R. Dallier[33, 32], B. Daniel[17],
S. Dasso[5, 3], K. Daumiller[36], B.R. Dawson[12], R.M. de Almeida[23], S.J. de Jong[59, 61], G. De Mauro[59],
J.R.T. de Mello Neto[22], I. De Mitri[47], J. de Oliveira[23], V. de Souza[15], L. del Peral[73], O. Deligny[28],
H. Dembinski[36], N. Dhital[84], C. Di Giulio[44], A. Di Matteo[48], J.C. Diaz[84], M.L. Díaz Castro[17],
F. Diogo[65], C. Dobrigkeit [17], W. Docters[60], J.C. D'Olivo[58], A. Dorofeev[79], Q. Dorosti
Hasankiadeh[36], M.T. Dova[4], J. Ebr[26], R. Engel[36], M. Erdmann[39], M. Erfani[41], C.O. Escobar[82, 17],
J. Espadanal[65], A. Etchegoyen[8, 11], H. Falcke[59, 62, 61], K. Fang[89], G. Farrar[85], A.C. Fauth[17],
N. Fazzini[82], A.P. Ferguson[77], M. Fernandes[22], B. Fick[84], J.M. Figueira[8], A. Filevich[8],
A. Filipčič[70, 71], B.D. Fox[90], O. Fratu[69], M.M. Freire[6], B. Fuchs[35], T. Fujii[89], B. García[7],
D. Garcia-Pinto[72], F. Gate[33], H. Gemmeke[37], A. Gherghel-Lascu[66], P.L. Ghia[30], U. Giaccari[22],
M. Giammarchi[42], M. Giller[64], D. Głas[64], C. Glaser[39], H. Glass[82], G. Golup[1], M. Gómez Berisso[1],
P.F. Gómez Vitale[10], N. González[8], B. Gookin[79], J. Gordon[87], A. Gorgi[52], P. Gorham[90],
P. Gouffon[16], N. Griffith[87], A.F. Grillo[51], T.D. Grubb[12], F. Guarino[43], G.P. Guedes[18],
M.R. Hampel[8], P. Hansen[4], D. Harari[1], T.A. Harrison[12], S. Hartmann[39], J.L. Harton[79],
A. Haungs[36], T. Hebbeker[39], D. Heck[36], P. Heimann[41], A.E. Herve[36], G.C. Hill[12], C. Hojvat[82],
N. Hollon[89], E. Holt[36], P. Homola[34], J.R. Hörandel[59, 61], P. Horvath[27], M. Hrabovský[27, 26],
D. Huber[35], T. Huege[36], A. Insolia[45], P.G. Isar[67], I. Jandt[34], S. Jansen[59, 61], C. Jarne[4],
J.A. Johnsen[78], M. Josebachuili[8], A. Kääpä[34], O. Kambeitz[35], K.H. Kampert[34], P. Kasper[82],
I. Katkov[35], B. Kégl[29], B. Keilhauer[36], A. Keivani[88], E. Kemp[17], R.M. Kieckhafer[84], H.O. Klages[36],
M. Kleifges[37], J. Kleinfeller[9], R. Krause[39], N. Krohm[34], O. Krömer[37], D. Kuempel[39], N. Kunka[37],
D. LaHurd[77], L. Latronico[52], R. Lauer[92], M. Lauscher[39], P. Lautridou[33], S. Le Coz[31], D. Lebrun[31],
P. Lebrun[82], M.A. Leigui de Oliveira[21], A. Letessier-Selvon[30], I. Lhenry-Yvon[28], K. Link[35],
L. Lopes[65], R. López[53], A. López Casado[75], K. Louedec[31], L. Lu[34, 76], A. Lucero[8], M. Malacari[12],
S. Maldera[52], M. Mallamaci[42], J. Maller[33], D. Mandat[26], P. Mantsch[82], A.G. Mariazzi[4], V. Marin[33],
I.C. Mariş[74], G. Marsella[47], D. Martello[47], L. Martin[33, 32], H. Martinez[54], O. Martínez Bravo[53],
D. Martraire[28], J.J. Masías Meza[3], H.J. Mathes[36], S. Mathys[34], J. Matthews[83], J.A.J. Matthews[92],
G. Matthiae[44], D. Maurel[35], D. Maurizio[13], E. Mayotte[78], P.O. Mazur[82], C. Medina[78],
G. Medina-Tanco[58], R. Meissner[39], V.B.B. Mello[22], D. Melo[8], A. Menshikov[37], S. Messina[60],
R. Meyhandan[90], M.I. Micheletti[6], L. Middendorf[39], I.A. Minaya[72], L. Miramonti[42], B. Mitrica[66],
L. Molina-Bueno[74], S. Mollerach[1], F. Montanet[31], C. Morello[52], M. Mostafá[88], C.A. Moura[21],
M.A. Muller[17, 20], G. Müller[39], S. Müller[36], R. Mussa[46], G. Navarra[52] ‡, S. Navas[74], P. Necesal[26],
L. Nellen[58], A. Nelles[59, 61], J. Neuser[34], D. Newton[75 b], P.H. Nguyen[12], M. Niculescu-Oglinzanu[66],
M. Niechciol[41], L. Niemietz[34], T. Niggemann[39], D. Nitz[84], D. Nosek[25], V. Novotny[25], L. Nožka[27],
L. Ochilo[41], F. Oikonomou[88], A. Olinto[89], V.M. Olmos-Gilbaja[75], N. Pacheco[73], D. Pakk
Selmi-Dei[17], M. Palatka[26], J. Pallotta[2], P. Papenbreer[34], G. Parente[75], A. Parra[53], T. Paul[81, 86],
M. Pech[26], J. Pękala[63], R. Pelayo[55], I.M. Pepe[19], L. Perrone[47], E. Petermann[91], C. Peters[39],
S. Petrera[48, 49], Y. Petrov[79], J. Phuntsok[88], R. Piegaia[3], T. Pierog[36], P. Pieroni[3], M. Pimenta[65],
V. Pirronello[45], M. Platino[8], M. Plum[39], A. Porcelli[36], C. Porowski[63], R.R. Prado[15], P. Privitera[89],

M. Prouza[26], V. Purrello[1], E.J. Quel[2], S. Querchfeld[34], S. Quinn[77], J. Rautenberg[34], O. Ravel[33],
D. Ravignani[8], B. Revenu[33], J. Ridky[26], S. Riggi[45], M. Risse[41], P. Ristori[2], V. Rizi[48], W. Rodrigues
de Carvalho[75], G. Rodriguez Fernandez[44], J. Rodriguez Rojo[9], M.D. Rodríguez-Frías[73],
D. Rogozin[36], J. Rosado[72], M. Roth[36], E. Roulet[1], A.C. Rovero[5], S.J. Saffi[12], A. Saftoiu[66],
F. Salamida[28], H. Salazar[53], A. Saleh[71], F. Salesa Greus[88], G. Salina[44], F. Sánchez[8],
P. Sanchez-Lucas[74], E. Santos[17], E.M. Santos[16], F. Sarazin[78], B. Sarkar[34], R. Sarmento[65], R. Sato[9],
C. Scarso[9], M. Schauer[34], V. Scherini[47], H. Schieler[36], P. Schiffer[40], D. Schmidt[36], O. Scholten[60] [a],
H. Schoorlemmer[90], P. Schovánek[26], F.G. Schröder[36], A. Schulz[36], J. Schulz[59], J. Schumacher[39],
S.J. Sciutto[4], A. Segreto[50], M. Settimo[30], A. Shadkam[83], R.C. Shellard[13], I. Sidelnik[1], G. Sigl[40],
O. Sima[68], A. Śmiałkowski[64], R. Šmída[36], G.R. Snow[91], P. Sommers[88], J. Sorokin[12], R. Squartini[9],
Y.N. Srivastava[86], D. Stanca[66], S. Stanič[71], J. Stapleton[87], J. Stasielak[63], M. Stephan[39], A. Stutz[31],
F. Suarez[8], T. Suomijärvi[28], A.D. Supanitsky[5], M.S. Sutherland[87], J. Swain[86], Z. Szadkowski[64],
O.A. Taborda[1], A. Tapia[8], A. Tepe[41], V.M. Theodoro[17], C. Timmermans[61, 59], C.J. Todero
Peixoto[14], G. Toma[66], L. Tomankova[36], B. Tomé[65], A. Tonachini[46], G. Torralba Elipe[75], D. Torres
Machado[22], P. Travnicek[26], R. Ulrich[36], M. Unger[85], M. Urban[39], J.F. Valdés Galicia[58], I. Valiño[75],
L. Valore[43], G. van Aar[59], P. van Bodegom[12], A.M. van den Berg[60], S. van Velzen[59], A. van Vliet[40],
E. Varela[53], B. Vargas Cárdenas[58], G. Varner[90], R. Vasquez[22], J.R. Vázquez[72], R.A. Vázquez[75],
D. Veberič[36], V. Verzi[44], J. Vicha[26], M. Videla[8], L. Villaseñor[57], B. Vlcek[73], S. Vorobiov[71],
H. Wahlberg[4], O. Wainberg[8, 11], D. Walz[39], A.A. Watson[76], M. Weber[37], K. Weidenhaupt[39],
A. Weindl[36], F. Werner[35], A. Widom[86], L. Wiencke[78], H. Wilczyński[63], T. Winchen[34],
D. Wittkowski[34], B. Wundheiler[8], S. Wykes[59], L. Yang[71], T. Yapici[84], A. Yushkov[41], E. Zas[75],
D. Zavrtanik[71, 70], M. Zavrtanik[70, 71], A. Zepeda[54], Y. Zhu[37], B. Zimmermann[37], M. Ziolkowski[41]
and F. Zuccarello[45]

[1] *Centro Atómico Bariloche and Instituto Balseiro (CNEA-UNCuyo-CONICET), San Carlos de Bariloche, Argentina*
[2] *Centro de Investigaciones en Láseres y Aplicaciones, CITEDEF and CONICET, Argentina*
[3] *Departamento de Física, FCEyN, Universidad de Buenos Aires and CONICET, Argentina*
[4] *IFLP, Universidad Nacional de La Plata and CONICET, La Plata, Argentina*
[5] *Instituto de Astronomía y Física del Espacio (IAFE, CONICET-UBA), Buenos Aires, Argentina*
[6] *Instituto de Física de Rosario (IFIR) - CONICET/U.N.R. and Facultad de Ciencias Bioquímicas y Farmacéuticas U.N.R., Rosario, Argentina*
[7] *Instituto de Tecnologías en Detección y Astropartículas (CNEA, CONICET, UNSAM), and Universidad Tecnológica Nacional - Facultad Regional Mendoza (CONICET/CNEA), Mendoza, Argentina*
[8] *Instituto de Tecnologías en Detección y Astropartículas (CNEA, CONICET, UNSAM), Buenos Aires, Argentina*
[9] *Observatorio Pierre Auger, Malargüe, Argentina*
[10] *Observatorio Pierre Auger and Comisión Nacional de Energía Atómica, Malargüe, Argentina*
[11] *Universidad Tecnológica Nacional - Facultad Regional Buenos Aires, Buenos Aires, Argentina*
[12] *University of Adelaide, Adelaide, S.A., Australia*
[13] *Centro Brasileiro de Pesquisas Fisicas, Rio de Janeiro, RJ, Brazil*
[14] *Universidade de São Paulo, Escola de Engenharia de Lorena, Lorena, SP, Brazil*
[15] *Universidade de São Paulo, Instituto de Física de São Carlos, São Carlos, SP, Brazil*
[16] *Universidade de São Paulo, Instituto de Física, São Paulo, SP, Brazil*
[17] *Universidade Estadual de Campinas, IFGW, Campinas, SP, Brazil*
[18] *Universidade Estadual de Feira de Santana, Brazil*
[19] *Universidade Federal da Bahia, Salvador, BA, Brazil*
[20] *Universidade Federal de Pelotas, Pelotas, RS, Brazil*
[21] *Universidade Federal do ABC, Santo André, SP, Brazil*
[22] *Universidade Federal do Rio de Janeiro, Instituto de Física, Rio de Janeiro, RJ, Brazil*
[23] *Universidade Federal Fluminense, EEIMVR, Volta Redonda, RJ, Brazil*
[24] *Universidad Industrial de Santander, Bucaramanga, Colombia*
[25] *Charles University, Faculty of Mathematics and Physics, Institute of Particle and Nuclear Physics, Prague, Czech Republic*
[26] *Institute of Physics of the Academy of Sciences of the Czech Republic, Prague, Czech Republic*
[27] *Palacky University, RCPTM, Olomouc, Czech Republic*

[28] *Institut de Physique Nucléaire d'Orsay (IPNO), Université Paris 11, CNRS-IN2P3, Orsay, France*

[29] *Laboratoire de l'Accélérateur Linéaire (LAL), Université Paris 11, CNRS-IN2P3, France*

[30] *Laboratoire de Physique Nucléaire et de Hautes Energies (LPNHE), Universités Paris 6 et Paris 7, CNRS-IN2P3, Paris, France*

[31] *Laboratoire de Physique Subatomique et de Cosmologie (LPSC), Université Grenoble-Alpes, CNRS/IN2P3, France*

[32] *Station de Radioastronomie de Nançay, Observatoire de Paris, CNRS/INSU, France*

[33] *SUBATECH, École des Mines de Nantes, CNRS-IN2P3, Université de Nantes, France*

[34] *Bergische Universität Wuppertal, Wuppertal, Germany*

[35] *Karlsruhe Institute of Technology - Campus South - Institut für Experimentelle Kernphysik (IEKP), Karlsruhe, Germany*

[36] *Karlsruhe Institute of Technology - Campus North - Institut für Kernphysik, Karlsruhe, Germany*

[37] *Karlsruhe Institute of Technology - Campus North - Institut für Prozessdatenverarbeitung und Elektronik, Karlsruhe, Germany*

[38] *Max-Planck-Institut für Radioastronomie, Bonn, Germany*

[39] *RWTH Aachen University, III. Physikalisches Institut A, Aachen, Germany*

[40] *Universität Hamburg, Hamburg, Germany*

[41] *Universität Siegen, Siegen, Germany*

[42] *Università di Milano and Sezione INFN, Milan, Italy*

[43] *Università di Napoli "Federico II" and Sezione INFN, Napoli, Italy*

[44] *Università di Roma II "Tor Vergata" and Sezione INFN, Roma, Italy*

[45] *Università di Catania and Sezione INFN, Catania, Italy*

[46] *Università di Torino and Sezione INFN, Torino, Italy*

[47] *Dipartimento di Matematica e Fisica "E. De Giorgi" dell'Università del Salento and Sezione INFN, Lecce, Italy*

[48] *Dipartimento di Scienze Fisiche e Chimiche dell'Università dell'Aquila and INFN, Italy*

[49] *Gran Sasso Science Institute (INFN), L'Aquila, Italy*

[50] *Istituto di Astrofisica Spaziale e Fisica Cosmica di Palermo (INAF), Palermo, Italy*

[51] *INFN, Laboratori Nazionali del Gran Sasso, Assergi (L'Aquila), Italy*

[52] *Osservatorio Astrofisico di Torino (INAF), Università di Torino and Sezione INFN, Torino, Italy*

[53] *Benemérita Universidad Autónoma de Puebla, Puebla, México*

[54] *Centro de Investigación y de Estudios Avanzados del IPN (CINVESTAV), México, México*

[55] *Unidad Profesional Interdisciplinaria en Ingeniería y Tecnologías Avanzadas del Instituto Politécnico Nacional (UPIITA-IPN), México, D.F., México*

[56] *Universidad Autónoma de Chiapas, Tuxtla Gutiérrez, Chiapas, México*

[57] *Universidad Michoacana de San Nicolás de Hidalgo, Morelia, Michoacán, México*

[58] *Universidad Nacional Autónoma de México, México, D.F., México*

[59] *IMAPP, Radboud University Nijmegen, Netherlands*

[60] *KVI - Center for Advanced Radiation Technology, University of Groningen, Netherlands*

[61] *Nikhef, Science Park, Amsterdam, Netherlands*

[62] *ASTRON, Dwingeloo, Netherlands*

[63] *Institute of Nuclear Physics PAN, Krakow, Poland*

[64] *University of Łódź, Łódź, Poland*

[65] *Laboratório de Instrumentação e Física Experimental de Partículas - LIP and Instituto Superior Técnico - IST, Universidade de Lisboa - UL, Portugal*

[66] *'Horia Hulubei' National Institute for Physics and Nuclear Engineering, Bucharest- Magurele, Romania*

[67] *Institute of Space Sciences, Bucharest, Romania*

[68] *University of Bucharest, Physics Department, Romania*

[69] *University Politehnica of Bucharest, Romania*

[70] *Experimental Particle Physics Department, J. Stefan Institute, Ljubljana, Slovenia*

[71] *Laboratory for Astroparticle Physics, University of Nova Gorica, Slovenia*

[72] *Universidad Complutense de Madrid, Madrid, Spain*

[73] *Universidad de Alcalá, Alcalá de Henares, Madrid, Spain*

[74] *Universidad de Granada and C.A.F.P.E., Granada, Spain*

[75] *Universidad de Santiago de Compostela, Spain*

[76] *School of Physics and Astronomy, University of Leeds, United Kingdom*

[77] *Case Western Reserve University, Cleveland, OH, U.S.A.*

[78] *Colorado School of Mines, Golden, CO, U.S.A.*

[79] *Colorado State University, Fort Collins, CO, U.S.A.*

[80] *Colorado State University, Pueblo, CO, U.S.A.*

[81] *Department of Physics and Astronomy, Lehman College, City University of New York, NY, U.S.A.*

[82] *Fermilab, Batavia, IL, U.S.A.*

[83] *Louisiana State University, Baton Rouge, LA, U.S.A.*

[84] *Michigan Technological University, Houghton, MI, U.S.A.*

[85] *New York University, New York, NY, U.S.A.*

[86] *Northeastern University, Boston, MA, U.S.A.*

[87] *Ohio State University, Columbus, OH, U.S.A.*

[88] *Pennsylvania State University, University Park, PA, U.S.A.*

[89] *University of Chicago, Enrico Fermi Institute, Chicago, IL, U.S.A.*

[90] *University of Hawaii, Honolulu, HI, U.S.A.*

[91] *University of Nebraska, Lincoln, NE, U.S.A.*

[92] *University of New Mexico, Albuquerque, NM, U.S.A.*

[‡] *Deceased*

[a] *Also at Vrije Universiteit Brussels, Belgium*

[b] *Now at University of Liverpool, U.K.*